ГОДИШНИК НА УНИВЕРСИТЕТА ПО АРХИТЕКТУРА, СТРОИТЕЛСТВО И ГЕОДЕЗИЯ – СОФИЯ

ANNUAL OF THE UNIVERSITY OF ARCHITECTURE, CIVIL ENGINEERING AND GEODESY – SOFIA

XLV том vol. 2010–2012 св. fasc. II

POROSITY EFFECTS ON THE NON-LINEAR BEHAVIOUR OF CONCRETE

Andrey P. Jivkov[1]

Keywords: *Concrete; Pore space; X-ray tomography; Lattice model; Damage evolution; Non-linear behaviour*

Research area: *MSC 2000 74Rxx (Fracture and damage of materials)*

ABSTRACT

The effect of porosity on the mechanical behaviour of concrete is investigated with a novel lattice model of its microstructure. The model represents the concrete microstructure with a set of sites connected by elastically deformable bonds. The bonds contain pores acting as micro-crack initiators. The pores are assigned to bonds according to an experimental pore size distribution obtained with X-ray computed tomography. Local damage (micro-cracking) is simulated by bond failure dependent on local forces and pore sizes. The global material behaviour emerges from the evolution and the collective behaviour of these local damages. Model predictions are compared to several experimental load cases. Strong correlation between porosity, micro-crack evolution and stress-strain response is demonstrated, particularly at lower strains. Plasticity contribution is dominant at high strains. Thus, initial non-linearity is controlled by micro-cracking at existing defects (pores), while the non-linearity near concrete failure is a result of combined local damages and plasticity.

1. Introduction

This work is part of an ongoing research programme on the performance of cement-based materials for nuclear plant and radwaste application. In some cases such materials will have predominantly radionuclide retaining function (e.g. wasteforms, backfills) and in others predominantly structural function (e.g. reactor cores, excavation support structures). For example, a critical role of a repository for radioactive waste is to ensure minimal release of

[1]Andrey P. Jivkov, The University of Manchester, School of Mechanical, Aerospace and Civil Engineering, Manchester M13 9PL, UK; Tel: +44 (0)161 3063556; e-mail: andrey.jivkov@manchester.ac.uk

radioactive species to the geosphere over very long times. An engineering safety case would demand fundamental understanding of the long-term evolution of the macroscopic properties of these materials. Key to the retaining function of the repository is the evolution of the transport properties, such as permeability and diffusivity. These are dictated by the 3D pore space in the materials used, which is characterised by the sizes and the connectivity of the pores present (see e.g. [1]). Consequently, the evolution of the macroscopic transport properties is governed by changes in the pore space.

The ongoing programme aims at developing, and validating experimentally, predictive models for the evolution of transport properties with pore space changes. This entails a modelling approach based on a practical, sufficiently realistic and modifiable 3D pore space representation. These requirements can be met to a large extent by the so called pore network models, where the pore space is described by a system of pores with various sizes some of which are connected by throats with various sizes [2, 3]. Changes in the pore space may result from chemical, electrochemical or bacterial effects as well as from mechanical damage, such as micro-cracking. When the pore space changing mechanism is defined, the evolution of the macroscopic transport properties can be evaluated by linking the pore network model of the pore space to appropriate model for the selected mechanism [4]. This work focuses on the mechanically induced micro-cracking as a pore space changing mechanism in concrete. We seek a microstructure-informed 3D model, where the pore space is explicitly represented in terms of experimentally determined pore size distribution, which can be used to inform a pore network model on changes in pore connectivity. The link between the two models is not a subject of the work and will be reported in future communications.

Discrete lattice representation of the material microstructure seems to offer the most appropriate modelling strategy for linking the mechanical behaviour to the pore network models. This is a meso-scale approach, where the material is appropriately subdivided into cells and lattice sites are placed at the centres of the cells. From one side, it is a natural solid-phase counterpart to the discrete pore networks. From the other side, discrete lattices allow for studies of distributed damage (micro-cracks) without constitutive assumptions about crack paths and coalescences that would be needed in a continuum finite element modelling. The deformation of the represented continuum arises from the interactions between the lattice sites. These involve forces resisting relative displacements and moments resisting relative rotations between sites. Two conceptually similar approaches have been proposed to link local interactions to continuum response. In the first one, the local forces are related to the stresses in the continuum cell (see e.g. [5–8]). In the second one, the interactions are represented by structural beam elements (or bonds), the stiffness coefficients of which are determined by equating the strain energy in the discrete and the continuum cell (see e.g. [9–12]). In both cases explicit relations between local and continuum parameters can be established for regular lattices [13]. For irregular lattices, such as those based on random Voronoi tessellation of space, such relations can be established only in an average sense [14]. Regular lattices, however, remain attractive because of the higher computational efficiency and the ability to upscale results.

Most of the previous works on lattice modelling of concrete have used a 2D lattice with hexagonal unit cell [9–12, 15]. The reason is that this lattice can be made correspondent to isotropic elastic materials with Poisson's ratio of up to 1/4 in plane strain and up to 1/3 in plane stress [10,14], hence covering a relatively large class of engineering materials. The progress to 3D simulations has been hindered by the fact that the simple 3D lattices cannot be made correspondent to isotropic materials other than materials with zero Poisson's ratio. This is the case for the lattices based on HCP and FCC arrangements analysed in [14], where

each site has 12 coordinating equidistant neighbours. Similar analysis for the simple cubic arrangement shows that again only isotropic elasticity with zero Poisson's ratio can be represented. A bi-regular lattice, based on a truncated octahedron unit cell, has been recently shown to be able to represent any elastic material of practical interest [16]. This quality comes from the presence of bonds with two different lengths, the properties of which can be selected independently, and creates the opportunity for realistic 3D simulations of damage evolution. The lattice has been previously used in modelling 3D intergranular crack propagation for stress corrosion and fatigue studies in steels [17, 18].

The aim of this work is to demonstrate a relation between a microstructure parameter, the pore size distribution, and a macroscopic behaviour, the stress-strain response of concrete. The success of such a demonstration will support strongly the planned coupling of the mechanical and the transport models. As a first approximation the concrete is considered isotropic elastic and modelled with the novel bi-regular lattice. The concrete non-linear behaviour is thus attributed solely to the emergence of micro-cracks, represented by failures of lattice bonds. The bond failure is controlled by the forces in the bond and the size of a pore assigned to the bond. The pore sizes are assigned to the bonds according to experimentally determined pore size distribution. The mechanical properties of the concrete under several loading conditions are used to explore the model. The link between the pore size distribution and the stress-strain response of the concrete is clearly demonstrated. The difference between the experimental and the predicted behaviour, particularly at strains close to failure, is attributed to concrete plasticity, currently not included in the model. It is concluded, that for relatively small deformations of the concrete the elastic model presented here will be sufficient for predicting changes in the pore space.

2. Material and experimental methods

Concrete samples with the composition given in Table 1 were used for this study.

Table 1. Composition of the concrete used for this study (OPC – Ordinary Portland Cement, PFA – Pulverized Fuel Ash)

Constituent	OPC	PFA	Sand	Quartz 10 mm	Quartz 20 mm	Plasticiser SP4	Water
Mass Ratio	1	0.33	2.45	1.39	2.78	0.0006	0.56

2.1. Pore size distribution

Data for the pore size distribution was obtained using X-ray Computed Tomography (X-ray CT). A cylindrical concrete core with a diameter of 28 mm was analysed, using the Nikon 225kV Custom Bay at the Henry-Moseley X-ray Imaging Facility (HMXIF), The University of Manchester. For data acquisition, a 1.5 mm thick copper filter with accelerating voltage of 160 kV, and a beam current of 200 μA was chosen. 3142 radiographic projections over a 360^{o} rotation were obtained, with an acquisition time of 1000 ms per radiograph. The Metris CT pro software was employed for reconstructing a 3D volume, with corrections for centre shift, beam hardening and noise reduction. The Aviso Fire segmentation software [19] was used to obtain pore size distribution from the 3D data set. A region of interest (ROI) of 25.2 mm x 18 mm x 18 mm located at the centre of the cylindrical specimen was chosen to reduce possible artefacts that may arise from analysing the free surface and surface breaking pores of the sample. The ROI had a dimension of 1700

x 1200 x 1200 voxels (3D pixels) with a voxel size of ca. 15 μm, Fig. 1(a). By using the Nyquist-Shannon sampling theorem [20], and assuming at least three pixels per resolvable element, a minimum detectable pore diameter of 31.5 μm could be obtained in this study. The grey-scale value (GSV) distribution of the concrete contained 3 distinct peaks, with one of those peaks associated with porosity. A minima thresholding routine to differentiate porosity from the cement matrix and the aggregates was used, followed by a sensitivity analysis to inform about the accuracy of the pore threshold, Fig. 1(b). Increments of ±25 GSV with respect to the chosen pore threshold produced an error of less than two percent. The segmented voxels corresponding with the porous phase were then analysed using the Avizo XQuant Quantification tool in Avizo Fire. This routine analyses each voxel in the porous phase of the ROI to ascertain any connectivity to other voxels of the same phase. Voxels belonging to the same connected cluster are then grouped together, and the volume of these clusters is used to calculate an equivalent pore size diameter assuming spherical pore morphology. Further details on pore space analysis can be found in [21].

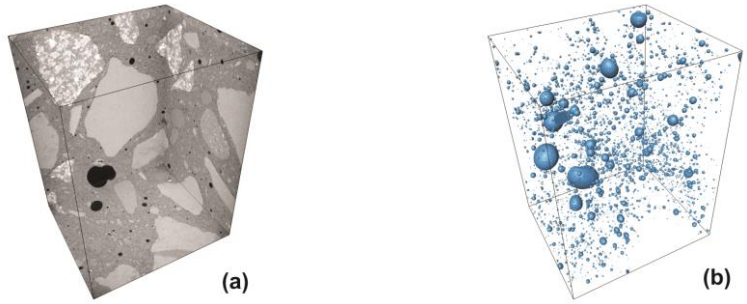

Figure 1. Reconstructed control specimen (a) and segmented porosity within the volume (b)

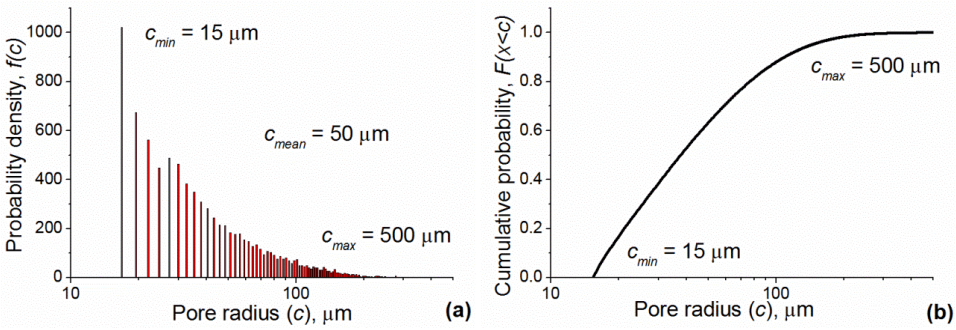

Figure 2. Statistical distributions of pore radii in the concrete: (a) probability density; (b) cumulative probability

Figure 2 shows the results for the probability density and cumulative probability of pore radii. The probability density histogram, Fig. 2(a), is determined by an optimised algorithm for bin-size selection [22] yielding a bin size of ca. 2.6 μm. The cumulative probability function, Fig. 2(b), is obtained with standard median ranking, where for pore radii ordered as $c_1 \leq c_2 \leq \ldots \leq c_n$, the cumulative probability for pores with radii less than c_i is given by $G(c < c_i) = (i - 0.3) / (n + 0.4)$. The number of pores measured experimentally is $n \approx 8900$. The minimum, maximum and average pore radii are depicted in Fig. 2. The cumulative

distribution function is used to populate the model described in Section 3 with pore sizes. This is done using a generator of uniformly distributed random numbers $0 \leq r < 1$, from which the pore radii are found as $c = G^{-1}(r)$.

2.2. Mechanical tests

All mechanical tests presented in this paper were carried out on cubic concrete specimens, in mac^{2T}, the facility for multi-axial compression of concrete at elevated temperature at The University of Sheffield [23]. The rig comprises three independent, orthogonal loading frames with 4MN capacity. The deformations of the specimens are obtained by the means of a system of 6 laser interferometers, measuring the positions of each of the 6 specimen surfaces. The load is applied via rigid, PTFE coated platens. Further details on the experimental procedure can be found in [24]. The concrete was cast in larger 130 mm thick slabs, then cut to 105 mm cubes, and machined (ground) to 100 mm right-regular cubic specimens that were used in the tests. All tests were performed at ambient temperature, using the following loading paths:

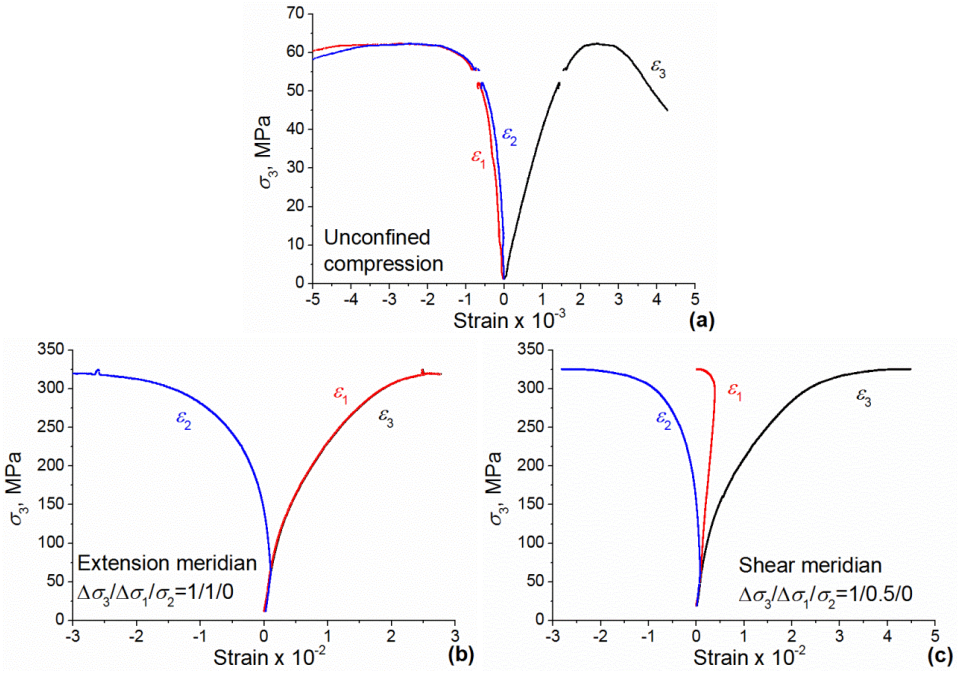

Figure 3. Experimental stress-strain behaviour of concrete: (a) unconfined uniaxial compression (Test 1); (b) extension meridian loading under confinement σ_2=61 MPa (Test 2); (c) shear meridian loading under confinement σ_2=61 MPa (Test 3)

Test 1: Unconfined uniaxial compression. This test was performed by increasing one principal stress (σ_3) monotonically to 80% of peak stress at a rate of 14.7 MPa/min, followed by strain control loading at 60 μm/min to the post-peak region. The other two stresses were kept constant at 1.0 MPa in order to maintain contact between the loading platens and the specimen, needed for the deformation measurements. Recorded stress-strain response is illustrated in Fig. 3(a).

Test 2: Extension meridian loading under confinement. This test was performed in two stages: (i) loading hydrostatically to confinement $p=\sigma_1=\sigma_2=\sigma_3=61$ MPa, (ii) keeping the minor stress σ_2 constant at 61 MPa (confinement) and increasing the two major stresses $\sigma_1=\sigma_3=p+\Delta\sigma$ to the peak, at the same stress/strain rates as in Test 1. Recorded stress-strain response is illustrated in Fig. 3(b).
Test 3: Shear meridian loading under confinement. This test was performed by following the same procedure as that in Test 2, except that in the second stage the major and the intermediate stress were different: $\sigma_3=p+\Delta\sigma$ and $\sigma_1=p+\Delta\sigma/2$. Recorded stress-strain response is illustrated in Fig. 3(c).
Test 4: Cyclic unconfined uniaxial compression. This test was performed by following the same procedure as that in Test 1, except that the major stress (σ_3) was applied in 3 loading-unloading cycles, between 1 MPa and 18, 30 and 42 MPa, before loading to the peak (at 60 MPa).
Test 5: Hydrostatic compression. This test was performed in 3 cycles, by loading $\sigma_1=\sigma_2=\sigma_3$ between 1 and 110 MPa, 220 MPa and 330MPa.

The elastic properties of the material were calculated from the unloading branches of cyclic uniaxial (unconfined) compression tests, (Test 4: Modulus of elasticity E = 46 GPa, and Poisson's ratio ν = 0.27), and hydrostatic compression tests (Test 5: Bulk modulus K = 33 GPa).

3. Modelling and simulations

3.1. Lattice model

Figure 4 illustrates the lattice model used in this work. The unit cell, shown in Fig. 4(a) is a truncated octahedron – a solid with six square and eight regular hexagonal boundaries. The 3D space can be compactly tessellated using such cells, with each cell representing a material meso-scale feature, e.g. grain, in an average sense. This representation is supported by physical and statistical arguments [16]. A discrete lattice is formed by placing sites at the centres of the cells and connecting each site to its 14 nearest neighbours; example is shown in Fig. 4(b).

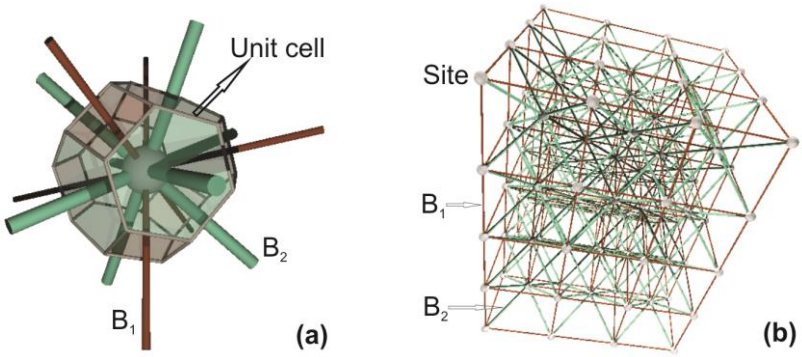

Figure 4. Lattice illustration: (a) unit cell (truncated octahedron) showing the site with 14 coordinating bonds – six in principal directions normal to squares (B_1) and eight in octahedral directions normal to hexagons (B_2); (b) discrete lattice of beam elements

The lattice contains two types of bonds. Bonds denoted by B_1 in Fig. 4 are normal to the square boundaries of the unit cell and form orthogonal set. For convenience this set is made coincident with the global coordinate system and B_1 are referred to as principal bonds. Bonds denoted by B_2 in Fig. 4 are normal to the hexagonal boundaries of the unit cell. The hexagons lie on the octahedral planes with respect to the selected system. Hence B_2 are referred to as octahedral bonds. If the spacing between sites in the three principal directions is denoted by L, bonds B_1 have length $L_1 = L$, and bonds B_2 have length $L_2 = \sqrt{3}\, L / 2$.

One important point about the proposed lattice is that it does not permit a simple closed form solution for the relation between bond properties and continuum elastic constants. In the general case, the behaviour of the two distinct types of bonds, B_1 and B_2, needs to be represented by eight parameters – normal, shear, twisting and bending stiffness for each bond type. With analysis based on equivalence of the energy in the continuum and the discrete unit cell, e.g. following [13], it can be shown that the proposed lattice represents a micropolar material with cubic elasticity. This is not surprising as the unit cell of the proposed model is the Voronoi cell (or the first Brillouin zone) of the face-centred cubic crystals. With analysis of a homogeneous displacement field, i.e. with no relative rotations between sites, the three constants of the cubic elasticity can be related to the four linear stiffness coefficients (normal and shear) of the bonds. Hence the model is over-determined, i.e. a particular set of continuum elastic constants can be achieved with infinite number of sets of bond stiffness coefficients. With analyses of more complex deformation modes involving relative rotations between sites, relations between the linear and the twisting/bending stiffness coefficients can be obtained. If such analyses are based on deformation energy functional dependent on strains only (classical continuum mechanics used in [13]) the problem remains over-determined. One possible explanation is that the proposed lattice arrangement is genuinely "micropolar", i.e. the stiffness coefficients of the bonds cannot be uniquely determined from classical strain energy potential. This is a subject of ongoing work and will be reported in a future publication.

The lattice, however, has been demonstrated to produce any predefined elastic response, including isotropic elasticity for a large class of materials [16]. This demonstration uses a "global" approach in the sense that the strain energy stored in the entire lattice is compared to the strain energy stored in a continuum with corresponding volume. It is assumed that for sufficiently large lattices the global approach provides satisfactory approximation with intrinsic micropolarity averaged over the volume. With this assumption it is convenient (and sufficient) to represent the bonds of the lattice with structural beam elements of circular cross sections, with R_1 and R_2 denoting the radii of beams B_1 and B_2, respectively. Assuming local isotropy, the modulus of elasticity, E_b, and the Poisson's ratio, ν_b, of the two types of beams should be the same. The four parameters, R_1 / L, R_2 / L, E_b, and ν_b can be calibrated so that the lattice produces the required isotropic elastic response. For the concrete studied in this work with $E = 46$ GPa and $\nu = 0.27$, the calibration following the procedure in [16] yields $R_1 / L = 0.2$; $R_2 / L = 0.32$; $E_b = 90$ GPa; and $\nu_b = 0.4$. These parameters are used for the simulations reported in the Section 4. The commercial software Abaqus [25] with Euler-Bernoulli beam formulation has been used. For the calibrated radius to length ratio of the beams, the use of the Timoshenko beam formulation would not offer noticeable improvement because the benefits are typically for ratios up to 1/8.

3.2. Failure criterion

Damage in the lattice model is introduced by removal of bonds. The criterion for bond failure is based on the forces and moments in the beam elements. This is formulated by

$$\frac{N}{N_f} + \frac{|S|}{S_f} + \alpha\frac{|T|}{T_f} + \alpha\frac{|M|}{M_f} \geq 1, \quad (1)$$

where N and S are the normal and shear forces in the beam, respectively; T and M are the twisting and the bending moments, respectively; N_f, S_f, T_f, and M_f are critical values of these forces and moments; and α is moments contribution factor. The normal force is taken with its sign – positive for tension and negative for compression. The shear force and the bending moment in Eq. (1) are obtained from the values in the two directions normal to the beam axis using the square root of squares rule. This criterion has been suggested previously to account for the contribution of all deformation modes to failure with $\alpha = 1$ [26]. Thus, a bond is permitted to fail under pure extension, pure shear, pure twist and pure bending separately, as well as under the combined action of the forces and moments. Taking only the first and the third term in Eq. (1) is principally equivalent to some of the previously used criteria, e.g. [9], where shear failure is not accounted for. Introducing the second and the third term allows for shear failure similarly to the way used in [11]. Note that in the current model failure may occur in a compressed bond provided that the other forces are sufficiently large to fulfil the criterion. If the sum of the first and fourth terms in Eq. (1) is larger than the sum of the second and third term, the failure is dominated by the normal stresses and we shall call this failure by separation. If the inverse is true, the failure is dominated by the shear stresses and we shall call this failure by sliding.

The failure parameters for the four modes, N_f, S_f, T_f, and M_f, can be related with the following argument [26]. For a beam of circular cross section of radius R, the failure stress corresponding to N_f is $\sigma_f = N_f / (\pi R^2)$; a tensile failure stress. The maximum stress due to bending is $\sigma_{max} = 4\ M / (\pi R^3)$. This equals the tensile failure stress for $M_f = N_f\ R / 4$. Similarly, the failure stress corresponding to S_f is $\tau_f = S_f / (\pi R^2)$; a shear failure stress. The maximum stress due to torsion is $\tau_{max} = 2\ T / (\pi R^3)$ and this equals the shear failure stress for $T_f = S_f\ R / 2$. With these relations between the failure moments and forces, the moment contribution factor, α, can have physical interpretation. It can be used as a measure of the position of a pore relative to the beam axis, so that α approaching zero corresponds to a pore close to the axis and α approaching one corresponds to a pore close to the beam surface. In this work $\alpha = 1$ has been used, i.e. the worst case scenario is assumed for the positions of all pores in the beams. Thus the failure criterion given by Eq. (1) requires two material parameters – the tensile and shear failure stresses, or equivalently failure forces. For convenience we introduce the parameter $\eta = S_f / N_f = \tau_f / \sigma_f$. Typical values for the shear to tensile strength ratio η are between one and two for quasi-brittle materials, with larger values yielding more brittle behaviour in uniaxial compression tests. This will be demonstrated by a parametric study in Section 4.

Key feature of the failure model is the relation between the tensile failure strength of a bond, σ_f, and the size of the pore assigned to the bond. This is based on the average stress criterion, proposed originally for circular holes (and cylindrical voids in 3D) [27]. According to this criterion, failure occurs when the average stress over a material dependent distance, d, reaches a critical value, σ_0. The material dependent parameter, d, is a function of, for example, pore space, aggregate size, cement grains, or hydrated/un-hydrated regions present in the cement matrix. The critical value can be interpreted as the "ideal" or "theoretical" tensile strength of the material, i.e. the strength without defects present. For convenience we introduce the non-dimensional parameter $\xi = c / (c + d)$, where c is the pore radius. In terms

of ξ the tensile failure strength of a bond with a spherical void is related to the "ideal" strength via [28]

$$\frac{\sigma_f}{\sigma_0} = \frac{2}{2+\xi(1+\xi)\left[\frac{2}{7}+\frac{9}{28}(1+\xi^2)\right]}. \quad (2)$$

Thus the failure model is based on three material dependent parameters: the material length scale, d; the "ideal" tensile strength, σ_0; and the shear to tensile strength ratio, η. The material length scale is expected to be of the order of the smallest pore size. Parametric study, shown in Section 4, suggests that length scales around the smallest pore size have effect on the macroscopic response up to roughly the average pore size after which the effect is negligible.

3.3. Simulation details

With respect to a coordinate system (X_1, X_2, X_3), coincident with the principal bonds, a model of a cubic region ($20L$, $20L$, $20L$) has been used. The corresponding lattice contains 17261 sites and 113260 bonds – 49260 of type B_1 and 64000 of type B_2. Note that for this lattice, each of the boundary planes $X_1 = 0$, $X_1 = 20L$, $X_2 = 0$, $X_2 = 20L$, $X_3 = 0$, $X_3 = 20L$ contains 21×21 sites. Three loading cases have been simulated: the unconfined uniaxial compression (UC); the extension meridian loading (EM); and the shear meridian loading (SM). The lattice has been loaded via prescribed displacements corresponding to the strains measured experimentally. Let (U_1, U_2, U_3) are the displacements and (F_1, F_2, F_3) are the reaction forces of sites on the lattice boundaries with respect to the coordinate system (X_1, X_2, X_3). For all loading cases the following boundary conditions have been fixed: $U_1 = 0$ for sites on $X_1 = 0$; $U_2 = 0$ for sites on $X_2 = 0$; $U_3 = 0$ for sites on $X_3 = 0$.

For UC, the conditions for the remaining boundaries are: $F_1 = 0$ (free sites) on $X_1 = 20L$; $F_2 = 0$ (free sites) on $X_2 = 20L$; $U_3 = 20L\varepsilon_3(t)$ for sites on $X_3 = 20L$, where $\varepsilon_3(t)$ is the experimentally measured compressive strain evolution. The macroscopic stress in the loading direction is resolved as the ratio between the total reaction force at sites on $X_3 = 20L$ and the boundary area, i.e. $\sigma_3 = \Sigma F_3 / 400L^2$. The macroscopic strains in the lateral directions are taken as the ratios between the average displacements of sites on $X_1 = 20L$ on $X_2 = 20L$, and the model length, i.e. $\varepsilon_1 = \Sigma U_1 / (21^2 \times 20L)$ and $\varepsilon_2 = \Sigma U_2 / (21^2 \times 20L)$.

For EM and SM, the lattice has been initially subjected to hydrostatic compression with applied displacements: $U_1 = 20L\varepsilon(t)$ for sites on $X_1 = 20L$; $U_2 = 20L\varepsilon(t)$ for sites on $X_2 = 20L$; $U_3 = 20L\varepsilon(t)$ for sites on $X_3 = 20L$, where the compressive strain $\varepsilon(t)$ has been increased until the macroscopic boundary stresses $\sigma_1 = \sigma_2 = \sigma_3$ reached the confining pressure $p = 61$ MPa as in experiment. The reaction forces at sites on $X_2 = 20L$ are recorded for the next loading step as $F_2(p)$. Within this, the boundary conditions have been changed to: $U_1 = 20L\varepsilon_1(t)$ for sites on $X_1 = 20L$; $U_3 = 20L\varepsilon_3(t)$ for sites on $X_3 = 20L$; $F_2 = F_2(p)$ for sites on $X_2 = 20L$. Here, $\varepsilon_1(t)$ and $\varepsilon_3(t)$ are the experimentally measured compressive strain evolutions. The macroscopic stresses σ_1 and σ_3 are determined as above, while $\sigma_2 = 61$ MPa. The macroscopic strain ε_2 is determined as above.

The simulations have been performed with an in-house code controlling the failure of bonds and interfacing with Abaqus, which is used for solving the lattice equilibrium after each load increment. Variable load increments have been used, so that a single failure event occurs within one increment. This is based on the standard cut-back algorithm used in plasticity. Together with the emergent macroscopic behaviour (stress versus strain), the

failure events and their nature (separation versus sliding) have also been recorded for the bonds in all lattice directions. The model has been calibrated using the unconfined uniaxial compression loading case. We define the "ideal" tensile strength, σ_0, to be the value for which the maximum stress in the simulations equals the maximum stress in the experiment, see Fig. 3(a). This depends on the selected material length scale, d, and the shear to tensile strength ratio, η, which is shown by parametric studies in Section 4. A particular selection of the three parameters is used for the simulations of the extension and the shear meridian loading cases. This is given by $d = 40$ μm and $\eta = 2$, for which the calibrated "ideal" tensile strength is $\sigma_0 = 28$ MPa. The selection is related to the outcomes from the parametric studies under unconfined uniaxial compression.

4. Results

All results presented in this section are obtained with one and the same distribution of pore sizes within the bonds. Statistical analysis of the model responses for various distributions is outside the scope of the present work. In all figures presented, the strains and stresses are assumed positive if compressive and negative if tensile.

4.1. Unconfined uniaxial compression: effect of material length scale

Figure 5 shows the results of the simulations performed to study the effect of the material length scale, d, with fixed shear to tensile strength ratio and ideal tensile strength as depicted. The macroscopic stress in the direction of the applied displacement is plotted versus the macroscopic strain. The experimental stress-strain behaviour is shown for comparison with broken line. The four values of d, depicted in the figure, are selected from less than the minimum pore size (15 μm) up to the average pore size (50 μm). The simulated behaviour follows closely the experiment for sufficiently small strains. The effect of smaller length scales is in the reduction of the predicted peak stress after which softening occurs. For the results in Fig. 5, the ideal strength is selected such that the peak stress for the case $d = 40$ μm equals the experimental one. Hence, a smaller length scale requires a larger ideal tensile strength value to match the experimental behaviour. However, the effect of the length scale diminishes for $d > 50$ μm (the average pore size) as seen by comparing the curves for $d = 40$ μm and $d = 50$ μm.

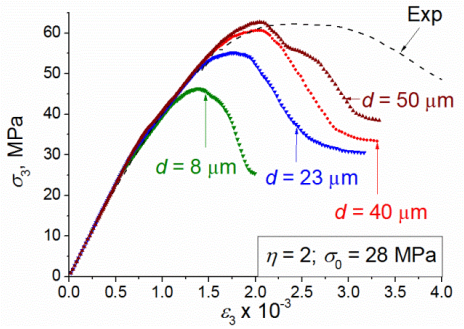

Figure 5. Simulated stress-strain behaviour of concrete under unconfined uniaxial compression: Effect of material length scale (depicted on curves) for fixed ideal tensile strength and shear to tensile strength ratio (depicted on graph)

The micro-cracking within the volume studied is initially randomly distributed. It is therefore convenient to represent the development of damage as fractions of failed bonds relative to the total number of bonds in the model. Figure 6 shows the fractions of bonds failed by separation (a) and by sliding (b) for the four length scale cases presented in Fig. 5. The point of peak stress recorded for each length scale case is shown with a star on the corresponding curve. These curves show that the evolution of damage commences with rapid increase of separation cracks which flattens out with the onset of sliding cracks; compare Fig. 6(a) with Fig. 6(b). The number of separation cracks at peak stress (onset of softening behaviour) is nearly independent of the material length scale selected, Fig. 6(a); the peak stress occurs at the inflection points of the curves. The post-peak (softening) behaviour is characterised with a rapid increase of sliding micro-cracks, Fig. 6(b), and continuing but moderate increase of separation micro-cracks, Fig. 6(a). There is a small effect of the material length scale on the sliding failures at peak stress, Fig. 6(b), however, this diminishes with increasing the length scale. Although the post-peak behaviour is still affected by the material length scale, we choose the case $d = 40$ μm as basic for the subsequent parametric studies and analysis.

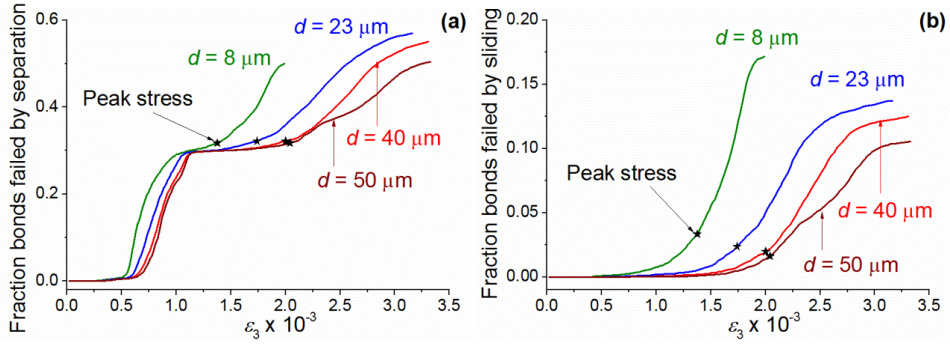

Figure 6. Evolution of damage (micro-cracks) under unconfined uniaxial compression, represented with fractions of failed bonds out of all bonds in the model: (a) separation micro-cracks; (b) sliding micro-cracks. The points of recorded peak stress are shown with stars on the four length scale cases curves

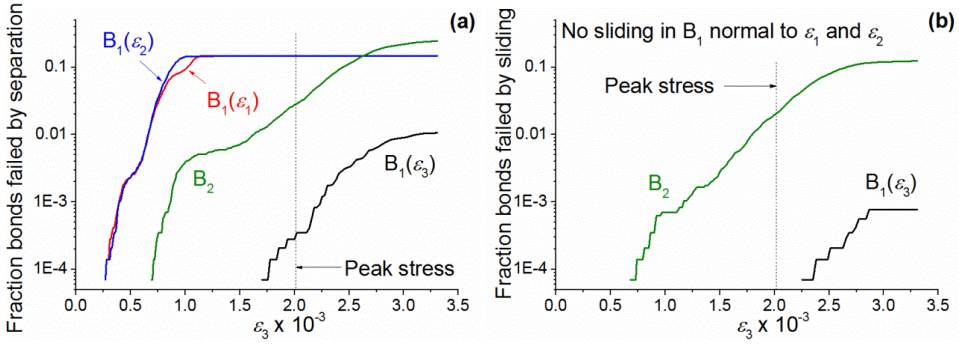

Figure 7. Evolution of micro-cracks under unconfined uniaxial compression, represented with fractions of failed bonds out of all bonds in the model: (a) separation micro-cracks on principal and octahedral planes; (b) sliding micro-cracks on principal and octahedral planes

To further illustrate the nature and orientation of the distributed micro-cracks, the separation and sliding failures normal to the principal and octahedral directions are considered for the basic case with d = 40 μm, η = 2, and σ_0 = 28 MPa. Figure 7 shows the results for separation micro-cracks (a) and sliding micro-cracks (b). The principal bonds in the unconfined directions, i.e. those parallel to ε_1 and ε_2, and denoted by $B_1(\varepsilon_1)$ and $B_1(\varepsilon_2)$, respectively, develop exclusively separation micro-cracks and fail rapidly during the initial stages of straining; see Fig. 7(a) and Fig. 7(b). These are followed by rapid growth of separation and sliding failures on the octahedral planes, denoted by B_2. A small number of separation and sliding micro-cracks develop also in the principal bonds parallel to the loading direction, denoted by $B_1(\varepsilon_3)$. These form around and after the peak during the softening and are apparently due to excessive bending contribution in the failure criterion.

Figure 8 shows the prediction of the model for both the compressive and the lateral strains compared to the experimental measurement shown in Fig. 3(a). The development of the strain in the unconfined direction is in a very good agreement with experiment up to strains very close to the peak of the response. This supports strongly the capability of the proposed model to simulate the pre-peak macroscopic behaviour based on the elastic calibration of the lattice and the development of distributed failures governed by the sizes of the pores. The post-peak behaviour of the compressive and the lateral strains cannot be reproduced correctly. This suggests that other types of non-linearities become dominating, e.g. plastic behaviour and geometry effects during testing.

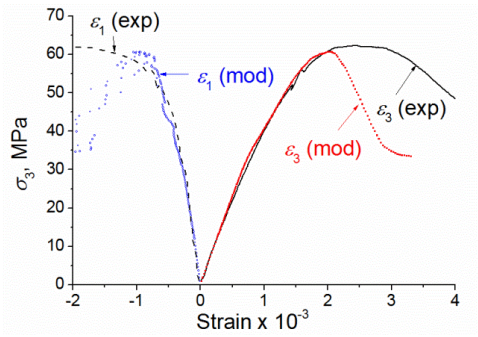

Figure 8. Simulated stress-strain behaviour of concrete under unconfined uniaxial compression: strains in compression and unconfined directions. Results for the basic selection of model parameters depicted

4.2. Unconfined uniaxial compression: effect of shear to tensile strength ratio

Figure 9 shows the results of the simulations performed to study the effect of the shear to tensile strength ratio, η, with fixed material length scale and ideal tensile strength as depicted. Typical values of η are studied, including η = 2 shown before in Fig. 5. The effect of η is similar in nature to the effect of material length scale, see Fig. 5. The peak stress is reached at lower strains for lower shear strength values. This suggests more brittle behaviour for materials with lower shear to tensile strength ratio. For known η < 2, the model can be recalibrated to find the ideal tensile strength, σ_0, for which the predicted peak stress equals the experimental one.

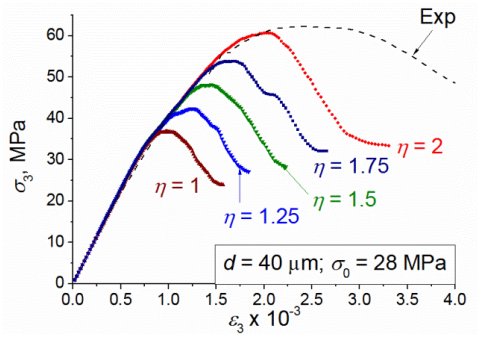

Figure 9. Simulated stress-strain behaviour of concrete under unconfined uniaxial compression: Effect of shear to tensile strength ratio (depicted on curves) for fixed material length scale and ideal tensile strength (depicted on graph)

The development of micro-cracks for different values of η is illustrated in Fig. 10. The curves in Fig. 10(a) show the fraction of bonds failed by separation and the curves in Fig. 10(b) show the fraction of bonds failed by sliding. These show that damage starts with rapid increase of separation failures, similarly to the observation in Fig. 6, which slows down after the onset of sliding failures. The increase of sliding failures dominates the response up to the peak stress with very little contribution of separation failures. The post-peak (softening) response is characterised by continuing rapid increase in sliding and moderate increase in separation failures. Notably, a reduction of the shear strength, i.e. decreasing η, leads to decreasing contribution of separation failures and increasing contribution of sliding failures near the peak stress and during softening. For sufficiently small strains, e.g. $\varepsilon_3 < 1\times10^{-3}$, the effect of η is negligible, Fig. 10(a). The behaviour is dominated by separation failures normal to the unconfined planes of the model and on octahedral planes, see Fig. 7(a).

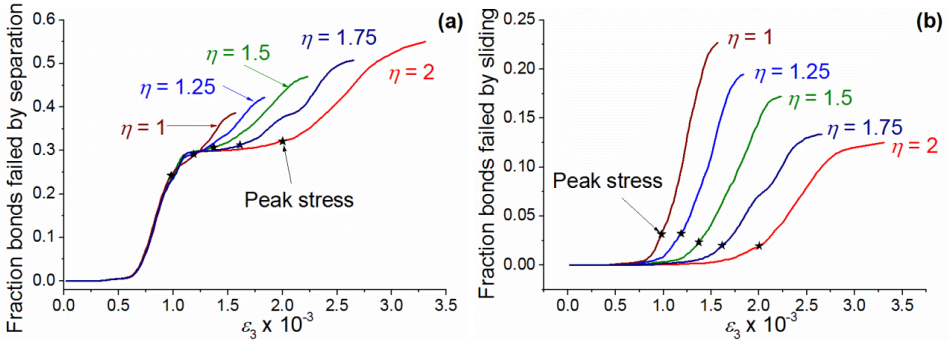

Figure 10. Evolution of micro-cracks under unconfined uniaxial compression, represented with fractions of failed bonds out of all bonds in the model: (a) separation micro-cracks; (b) sliding micro-cracks. The points of recorded peak stress are shown with stars on the four length scale cases curves

4.3. Complex loading: extension and shear meridians

Figure 11 shows the simulated response of the concrete under the extension meridian loading, compared to the experimentally measured response. The initial confining pressure and the model parameters used are depicted. The predicted responses are in very good

agreement with experiment for sufficiently small, but well above the confining, stresses. However, for larger strains the simulations show "stiffer" and more brittle response. This is an indication that the non-linearity introduced by the elastic micro-cracking model is not sufficient for describing the macroscopic behaviour at high stresses and strains. However, a significant part of the non-linear response can be attributed to micro-cracking.

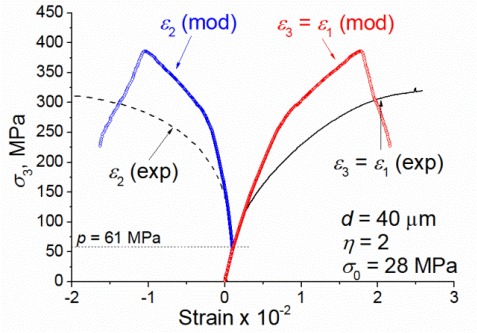

Figure 11. Simulated stress-strain behaviour of concrete under extension meridian loading: strains in compression and unconfined directions. Experimental curves (extension meridian loading under 61 MPa confinement) included for comparison. Model parameters and initial confining pressure depicted

Figure 12 shows the evolution of micro-cracking under the extension meridian loading leading to the emergent stress-strain response shown in Fig. 11. The notations in Fig. 12 are identical to the notations in Fig. 7. Notably, damage commences with rapid development of separation, Fig. 12(a), and sliding, Fig. 12(b), micro-cracks in bonds in the direction of constant stress, $B_1(\varepsilon_2)$. The damage continues with increase of the separation failures in the same bonds, Fig. 12(a), followed by rapid increase of sliding failures on octahedral planes, B_2, Fig. 12(b). This leads to the peak in the simulated stress response, see Fig. 11, after which the softening is characterised by increases in separation and sliding failures in the bonds in the directions of continuous loading, $B_1(\varepsilon_1)$ and $B_1(\varepsilon_3)$, and on octahedral planes, B_2. Although the simulations may not be representative for higher strains, the results in Fig. 12 provide useful information on the nature of micro-cracking. The observed behaviour is physically realistic and illustrates the potential of the model.

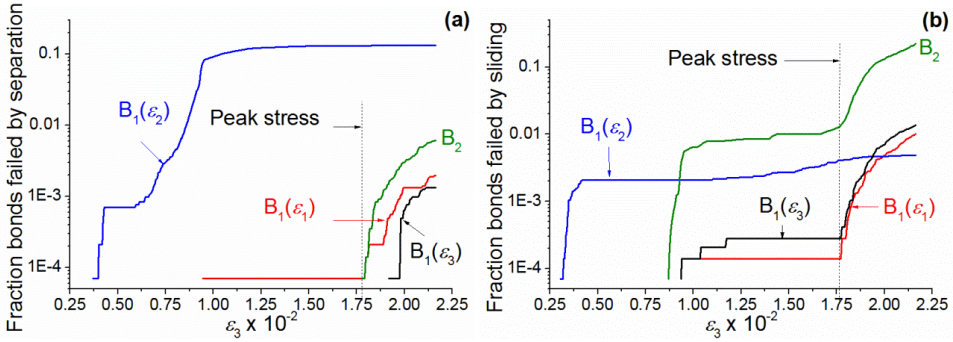

Figure 12. Evolution of micro-cracks under extension meridian loading, represented with fractions of failed bonds out of all bonds in the model: (a) separation micro-cracks on principal and octahedral planes; (b) sliding micro-cracks on principal and octahedral planes

Figure 13 presents the simulated response of the concrete under the shear meridian loading, compared to the experimentally measured response. The agreement with experiment for this loading case is somewhat better than the agreement for the extension meridian, Fig. 11. In particular, the strain in the direction of constant stress, ε_2, is in excellent agreement up to very high stresses. The responses are less stiff and brittle for all principal strains, suggesting that the contribution of the elastic micro-cracking to the overall non-linear response is larger under shear meridian loading than under extension meridian loading. The contribution of plasticity remains important at increasing strains.

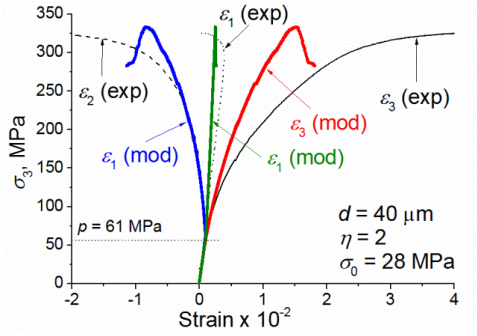

Figure 13. Simulated stress-strain behaviour of concrete under shear meridian loading: strains in all principal directions. Experimental curves (shear meridian loading under 61 MPa confinement) included for comparison. Model parameters and initial confining pressure depicted

Figure 14 illustrates the evolution of micro-cracking under the shear meridian loading leading to the emergent stress-strain response shown in Fig. 13. Damage commences with rapid development of separation, Fig. 14(a), and sliding, Fig. 14(b), micro-cracks in bonds in the direction of constant stress, $B_1(\varepsilon_2)$. This is followed by rapid increases in sliding failures on octahedral planes, B_2, and in bonds in the direction of the smaller increasing strain, $B_1(\varepsilon_1)$, Fig. 14(b). In parallel, the separation failures in $B_1(\varepsilon_2)$ continue to grow together with emerging separation failures in $B_1(\varepsilon_1)$, Fig. 14(a). This leads to the peak in the simulated stress response, Fig. 13, after which the softening is characterised by increases in separation and sliding failures in all bonds, including those along the larger increasing strain, $B_1(\varepsilon_3)$.

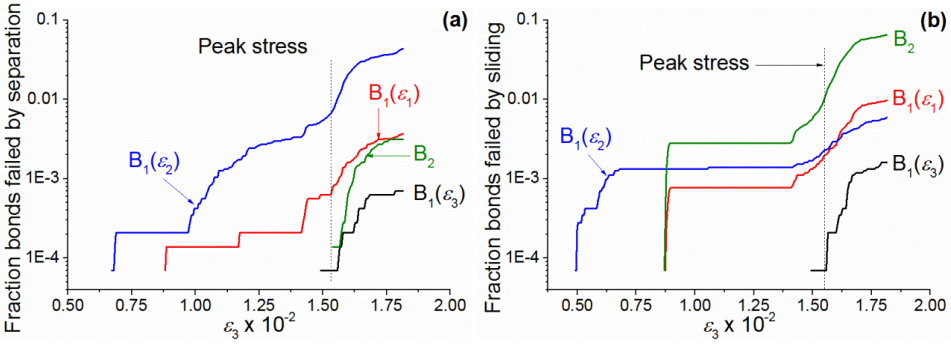

Figure 14. Evolution of micro-cracks under shear meridian loading, represented with fractions of failed bonds out of all bonds in the model: (a) separation micro-cracks on principal and octahedral planes; (b) sliding micro-cracks on principal and octahedral planes

Comparison between Fig. 14 and Fig. 12, shows that the shear meridian loading produces a more complex micro-crack population. The peak stress is reached due to separation and sliding failures in two principal directions in addition to sliding failures on octahedral planes. The biggest differences between the complex loading cases and the unconstrained uniaxial compression are: (i) for the confined cases separation failures on octahedral planes do not occur prior to softening (see B_2 in Figs. 12(a) and 14(a)), while for the unconfined case such failures contribute substantially to peak stress (see B_2 in Fig. 7(a)); and (ii) for the unconfined case sliding failures on the planes parallel to the load do not occur (see $B_1(\varepsilon_1)$ and $B_1(\varepsilon_2)$ in Fig. 7(b)), while for the confined cases such failures contribute to the peak stress (see $B_1(\varepsilon_1)$ and $B_1(\varepsilon_2)$ in Figs. 12(b) and 14(b)).

5. Discussion and conclusions

The model presented in this work is based on a linear elastic behaviour at the material meso-scale, i.e. linear elastic bonds. The non-linearity in the simulated macroscopic responses is solely due to elimination of bonds representing the emergence of micro-cracks. The criterion for bond elimination (failure) is based on the local forces and moments and on the size of a pore allocated to the bond. The pore size effect is accounted for using the average stress over a material distance, with failure occurring when this stress reaches a critical "ideal" strength.

The material distance, or length scale, is not known. However, it has been demonstrated that the effect of this parameter on the predicted response is significant only for values of the order of the smallest pores and diminishes quickly for values above the average pore size, see Fig. 5. The results suggest that smaller material length scales yield more brittle macroscopic responses, as the peak stress (onset of softening) is reached at lower strains. The pore size distribution measured experimentally, Fig. 2, represents the tail of the real distribution as pores of sizes below 15 μm have not been resolved. However, the average pore size will not change noticeably if the missing head of the distribution is included, e.g. by assuming a Weibull-continuation of the measured data. It could be reduced from the current 50 μm down to at most 40 μm. Hence, the results presented in this work will not change substantially with the inclusion of smaller pore sizes, provided that the material length scale is larger than the average pore size. However, if the material length scale is known from experiment to be smaller than the average pore size, the model can be recalibrated to find the "ideal" tensile strength for which the simulated response matches the experimental one.

The other parameter controlling the macroscopic behaviour is the shear to tensile strength ratio. Experimental value for this parameter is not available for the concrete studied in the work. Parametric studies with the typical values for quasi-brittle materials performed illustrate the effect of the shear strength. It has been shown that smaller shear strength values produce more brittle macroscopic responses, Fig. 9. Notably, for a known shear to tensile strength ratio, the model can be recalibrated to find the corresponding "ideal" tensile strength.

The "ideal" tensile strength is a model parameter representing the uniform tensile stress required to break a material volume with no defects present. Therefore it cannot be related to the experimentally determined tensile strength of the concrete in a simple manner. As the results suggest, it depends on the material length scale and the shear strength, Figs. 5 and 9. The value used in the work, $\sigma_0 = 28$ MPa, can be considered as a lower bound for the parametric studies performed. This is because any reduction of the shear strength, as well as

any reduction of the material length scale, would require an increase of σ_0 in order to simulate the experimental macroscopic response. Therefore the "ideal" tensile strength remains a calibrating parameter at the meso-scale. The model presented considers homogenised meso-scale properties, i.e. the solid phases of the concrete and their interactions are not accounted for separately. In principle, the model can be extended to include different σ_0 for the interactions between different phases, e.g. by assigning appropriate values to different bonds. However, for small differences in σ_0 for different phases, the effect will be negligible when compared to the effect of the sizes of the distributed pores. Nevertheless, this possibility should be explored in the future, in particular if the sizes of the pores are found to be correlated to the solid phases, e.g. part of the distribution is found predominantly in one phase.

The model realism is strongly supported by the results presented for the nature and orientation of micro-cracks. In the case of unconfined uniaxial compression, Figs. 6, 7, and 10 demonstrate that damage initiates by separation failures normal to the unconfined directions followed by separation failures on octahedral planes, Fig. 7(a). The rapid increase in separation micro-cracks is interrupted by the occurrence of sliding failures on octahedral planes. The onset of sliding failures can be considered as the compressive strength of the concrete, because the fast increase of these leads quickly to the peak stress in the simulated response. The post-peak behaviour is a well-defined material softening due to continuing rapid increase in sliding failures and a more moderate increase in separation failures. This observations correlate very well with the expected development of micro-cracking. The resulting macroscopic stress-strain response in the loading and lateral directions, Fig. 8, is in excellent agreement with the experimental measurement for strains up to the onset of sliding failures. This is despite the use of linear elastic behaviour at the meso-scale. This suggests that the unconfined compression behaviour is controlled predominantly by micro-cracking in the region before the compressive strength is reached. Within the peak stress and post-peak regions, characterised by rapid growth of sliding failures in the elastic model, the predictions for loading and lateral strains deviate from the experiment. This is an indication that the measured response cannot be attributed to brittle micro-cracking alone; it becomes dominated by other factors, such as plasticity and micro-rotations at the meso-scale.

The results for the complex loading cases, extension meridian and shear meridian after hydrostatic compression, provide further evidence that the model generates physically realistic evolution of micro-crack populations. The predicted stress-strain responses are also in good agreement with experiment at lower stresses. The disagreement at higher stresses can be attributed to plasticity of concrete. Generally the plastic deformations would reduce the forces and moments in bonds at a given macroscopic strain, which will lead to more moderate development of micro-cracks and thence to a predicted response closer to the experiment. However, the results illustrate the important contribution of micro-cracking to the non-linear response of the concrete. This can be used in developing a plasticity model at the meso-scale by comparing the elastic to the elastic-plastic micro-cracking evolution. Further, the complex loading tests are performed to stress levels significantly higher to those expected in concretes in an underground repository. After sealing such a repository, the principal stresses in the cement-based components will be comparable to the stresses in the near field geology. For a repository at a depth of 500–1000 m, for example, the maximum principal stress is of the order of 15–30 MPa; the other principal stresses being smaller. Hence, the concretes will be subjected to stress triaxiality within the elastic range. This could be amended by internally produced stresses due to gas generation for example and externally produced stresses due to small land motions. Unless a catastrophic event, such as an earthquake, occurs, the development of stresses would remain in the elastic region. For this

case the results of this work are sufficiently representative. This suggests that the elastic micro-cracking model can be used to inform pore space models about changes in connectivity leading to predictions for evolution of transport properties.

The general conclusions of this work are:

- 3D lattice modelling is a promising approach for correlating micro-structural properties to the macroscopic behaviour of concretes;
- Clear link between concrete porosity, in terms of experimentally determined pore size distribution, and the emergent stress-strain response is demonstrated;
- Non-linear response prior to the compressive strength of the concrete is dominated by brittle micro-cracking formed by local material separation;
- Other material non-linearity, e.g. plasticity, governs the behaviour after the onset of sliding micro-cracks in the current elastic model, for both uniaxial and triaxial loading cases.
- The elastic model is sufficient to inform pore network models about changes in pore connectivity for the stress levels expected in concrete in underground repository.

LITERATURE

1. *Bernabé, Y., M. Li, A. Maineult.* Permeability and pore connectivity: A new model based on network simulations. J. Geophys. Res. 115: B10203, 2010.
2. *Ioannidis, M. A., I. Chatzis.* Network modelling of pore structure and transport properties of porous media. Chem. Eng. Sci. 48: 951-972, 1993.
3. *Blunt, M. J., M. D. Jackson, M. Piri, P. H. Valvatne.* Detailed physics, predictive capabilities and macroscopic consequences for pore-network models of multiphase flow. Adv. Water Resour. 25: 1069-1089, 2002.
4. *Jivkov, A. P., C. Hollis, F. Etiese, P. J. Withers.* A novel architecture for pore network modelling with applications to permeability of porous media. J. Hydrol. to appear 2012.
5. *Bazant, Z.P., B.H. Oh.* Microplane model for progressive fracture of concrete and rock. J. Eng. Mech. 111: 559-582, 1985.
6. *Carol, I., M. Jirasek, Z. P. Bazant.* A thermodynamically consistent approach to microplane theory. Part I. Free energy and consistent microplane stress. Int. J. Solids Struct. 38: 2921-2931, 2001.
7. *Cusatis, G., Z. P. Bazant, L. Cedolin.* Confinement-shear lattice CSL model for fracture propagation in concrete. Comp. Meth. Appl. Mech. Eng. 195: 7154-7171, 2006.
8. *Cusatis, G., D. Pelessone, A. Mencarelli.* Lattice discrete particle model (LDPM) for failure behaviour of concrete. I: Theory. Cement Concr. Comp. 33: 881-890, 2011.
9. *Schlangen, E., J. G. M. van Mier.* Experimental and numerical analysis of micromechanisms of fracture of cement-based composites. Cement Concr. Compos. 14: 105-118, 1992.

10. *Griffiths, D. V., G. G. W. Mustoe.* Modelling of elastic continua using a grillage of structural elements based on discrete element concepts. Int. J. Numer. Meth. Eng. 50: 1759-1775, 2001.

11. *Chang, C. S., T. K. Wang, L. J. Sluys, J. G. M. van Mier.* Fracture modeling using a micro structural mechanics approach - I. Theory and formulation. Eng. Fract. Mech. 69: 1941-1958, 2002.

12. *Karihaloo, B. L., P. F. Shao, Q. Z. Xiao.* Lattice modelling of the failure of particle composites. Eng. Fract. Mech. 70: 2385-2406, 2003.

13. *Wang, Y., P. Mora.* Macroscopic elastic properties of regular lattices. J. Mech. Phys. Solids 56: 3459-3474, 2008.

14. *Grassl, P., M. Jirasek.* Meso-scale approach to modelling the fracture process zone in concrete subjected to uniaxial extension. Int. J. Solids Struct. 47: 957-68, 2010.

15. *Liu, J. X., Z. Y. Zhao, S. C. Deng, N. G. Liang.* Numerical investigation of crack growth in concrete subjected to compression by the generalised beam lattice model. Comput. Mech. 43: 277-295, 2009.

16. *Jivkov, A. P., J. R. Yates.* Elastic behaviour of a regular lattice for meso-scale modelling of solids. Int. J. Solids Struct. 49: 3089-3099, 2012.

17. *Jivkov, A. P., N. P. C. Stevens, T. J. Marrow*. A three-dimensional computational model for intergranular cracking. Comput. Mater. Sci. 38: 442–453, 2006.

18. *Jivkov, A. P., T. J. Marrow.* Rates of intergranular environment assisted cracking in three-dimensional model microstructures. Theor. Appl. Fract. Mech. 48: 187-202, 2007.

19. AVIZO Software - http://www.vsg3d.com/avizo/fire

20. *Jerri, A. J.* The Shannon Sampling Theorem - Its Various Extensions and Applications: A Tutorial Review. Proc. IEEE 65: 1565–1595, 1977.

21. *Stein, R. C., M. Petkovski, D. L. Engelberg, N. C. Hyatt, P. J. Withers, T. Lowe.* Detecting microstructural changes in concrete conditioned under thermo-mechanical loading using X-ray computed tomography. Proc. 2nd Int. Conf. Microdurability, Paper 53, Amsterdam, Netherlands, 2012.

22. *Shimazaki, H., S. Shinomoto.* A method for selecting the bin size of a time histogram. Neural Comput. 19: 1503-1527, 2007.

23. *Petkovski, M., R. S. Crouch, P. Waldron.* Apparatus for testing concrete under multiaxial compression at elevated temperature (mac^{2T}). Exp. Mech. 46: 387-398, 2006.

24. *Petkovski, M.* Effects of stress during heating on strength and stiffness of concrete at elevated temperature. Cement Concr. Res. 40: 1744-1755, 2010.

25. ABAQUS, 2011. User's Manual, Version 10.1 ed., Dassault Systemes.

26. *Wang, Y., S. Abe, S. Latham, P. Mora.* Implementation of particle-scale rotation in the 3D-lattice solid model. Pure Appl. Geophys. 163: 1769-1785, 2006.

27. *Whitney, J. M., R. J. Nuismer.* Stress fracture criteria for laminated composites containing stress concentrations. J. Compos. Mater. 8: 253-265, 1974.

28. *Ippolito, M., A. Mattoni, N. Pugno, L. Colombo.* Failure strength of brittle materials containing nanovoids. Phys. Rev. B 75: 224110(1-7), 2007.

Submitted: September, 2012

ВЛИЯНИЕ НА ПОРЬОЗНОСТТА ВЪРХУ НЕЛИНЕЙНОТО ПОВЕДЕНИЕ НА БЕТОНА

Андрей П. Живков[1]

Ключови думи: *бетон; порьозно пространство; рентгенова томография; решетъчен модел; развитие на повреди; нелинейно поведение.*

Научна област: *MSC 2000 74Rxx (пукнатини и разрушаване на материалите)*

РЕЗЮМЕ

Влиянието на порьозността върху механичното поведение на бетона е изследвано с помощта на нов решетъчен модел на неговата микроструктура. Моделът представя микроструктурата на бетона чрез множество от възли съединени с еластично деформируеми връзки. Връзките съдържат пори, които действат като създатели на микропукнатини. Порите са приписани на връзките според експериментално определено разпределение на размерите на порите, получено чрез изчислителна рентгенова томография. Всяка локална повреда (микронапукване) е симулирана чрез разрушаване на връзка, зависещо от локалните усилия и размер на пората. Глобалното поведение на материала възниква в следствие на развитието и на колективното поведение на тези локални повреди. Предвижданията на модела са сравнени с експериментални резултати от няколко случая на натоварване. Установена е силна зависимост между порьозността, развитието на микропукнатини и произтичащата връзка между напрежения и деформации. Тази зависимост е подчертана при по-малки деформации, докато приноса на пластичните деформации доминира при големи деформации. Така, началната нелинейност в поведението на бетона е контролирана от микронапукване около съществуващи дефекти (пори), докато нелинейността близо до точката на разрушение е резултат от едновременното действие на микроповреди и пластични деформации.

[1]Андрей Живков, The University of Manchester, School of Mechanical, Aerospace and Civil Engineering, Manchester M13 9PL, UK; Tel: +44 (0)161 3063765; E-mail: andrey.jivkov@manchester.ac.uk